



1 **Multi-scale analysis and Modeling of aeromagnetic data over the**  
2 **Bétaré-Oya area in the Eastern Cameroon, for structural evidences**  
3 **investigations.**

4 **Christian Emile Nyaban<sup>a</sup>; Théophile Ndougsa-Mbarga<sup>a, b\*</sup>; Marcelin Bikoro-Bi-Alou<sup>c</sup>;**  
5 **Stella Amina Manekeng Tadjouteu<sup>a</sup>; Stephane Patrick Assembe<sup>a, d</sup>**

6 <sup>a</sup>Postgraduate School of Sciences, Technologies & Geosciences, University of Yaoundé I, Yaoundé, Cameroon.

7 <sup>b</sup>Department of Physics, Advanced Teachers' Training College, University of Yaoundé I, P.O. Box 47 Yaoundé  
8 Cameroon.

9 <sup>c</sup>Department of Earth Sciences, Faculty of Science, University of Maroua, Maroua, Cameroon.

10 <sup>d</sup>Department of Physics, Faculty of Science, University of Bamenda, Bamenda, Cameroon.

11 Correspondence should be addressed to Ndougsa Mbarga Théophile; \*ndougsa@yahoo.fr

12

13 **ABSTRACT:**

14 This study was carried out in the Lom series in Cameroun, at the border with Central African  
15 Republic located between the latitudes 5°30'-6°N and the longitudes 13°30'-14°45'E. A multi-  
16 scale analysis of aeromagnetic data combining tilt derivative, Euler deconvolution, upward  
17 continuation and the 2.75D modelling was used. The following conclusion were drawn: 1-  
18 Several major families of faults were mapped. Their orientations are ENE-WSW, E-W, NW-  
19 SE, N-S with a NE-SW prevalence. The latter are predominantly sub-vertical with NW and SW  
20 dips and appear to be prospective for the future mining investigation. 2-The evidence of  
21 compression, folding and shearing axis, was concluded from superposition of null contours of  
22 the tilt-derivative and Euler deconvolution. The evidence of the local tectonics principally due  
23 to several deformation episodes (D1, D2 and D4) associated with NE-SW, E-W, and NW-SE  
24 events respectively. 3- Depths of interpreted faults ranges from 1000 to 3400 m. 4- Several  
25 linear structures correlating with known mylonitic veins were identified. These are associated  
26 with the Lom faults and represent the contacts between the Lom series and the granito-gneissic  
27 rocks; we concluded the intense foldings caused by senestral and dextral NE-SW and NW-SE



28 stumps; 5- We propose a structural model of the top of the crust (schists, gneisses, granites) that  
29 delineates principal intrusions (porphyroid granite, garnet gneiss, syenites, micaschists,  
30 Graphite and Garnet gneiss) responsible for the observed anomalies. The 2.75D modelling  
31 revealed; many faults with a depth greater than 1200 m and confirmed the observations from  
32 RTE-TMI, Tilt derivative and Euler deconvolution; 6- We developed lithologic profile of  
33 Betare Oya basin.

34 **Keywords: Aeromagnetic data, multi-scale analysis, 2.75D modelling, faults.**

## 35 **1. Introduction**

36 Magnetic method has a renewed interest for solid mineral, hydrocarbons, and geological  
37 researches. During data interpretation, the first crucial step is the removal of the effect of deep-  
38 seated structures from the observed total magnetic field to enhance shallow body signatures  
39 (Ndougsa et al., 2007). These shallow bodies are generally associated to magnetic minerals  
40 such as magnetite, hematite which are contained by iron ore deposit (Ndougsa et al., 2013). The  
41 second step is mapping causative body's edges, which is fundamental to the use of potential  
42 field data for geological mapping. The edge detection techniques are used to distinguish  
43 between different sizes and different depths of the geological discontinuities (Oruç et al., 2011).  
44 In the last few years, there have been several methods proposed to help normalizing the  
45 magnetic signatures in images. Cordell and Grauch, (1985) have suggested a method to locate  
46 horizontal extents of the sources from the maxima of horizontal gradient of the pseudo-gravity  
47 computed from the magnetic anomalies. Verduzco et al., (2004) developed tilt derivative from  
48 gravity or magnetic field anomaly maps using the horizontal gradient magnitude of the tilt  
49 derivative as an edge detector.

50 Salem et al., (2008) developed a new interpretation method for gridded magnetic data based  
51 on the tilt derivative, without specifying prior information about the nature of the source. In this  
52 article, we suggest another approach which consists in the location of vertical contacts by using  
53 the maxima and horizontal edge of tilt derivative.



54

## 55 **2. Geological and tectonic setting**

### 56 **2.1. Regional setting.**

57 The following structural domains can be distinguished in the Pan-African belt north of the  
58 Congo craton (Toteu et al., 2004; Fig. 1.A):

59 (a) A pre-collisional stage that includes the emplacement of pre-tectonic calc-alkaline  
60 granitoids (e.g., at 660-670 Ma);

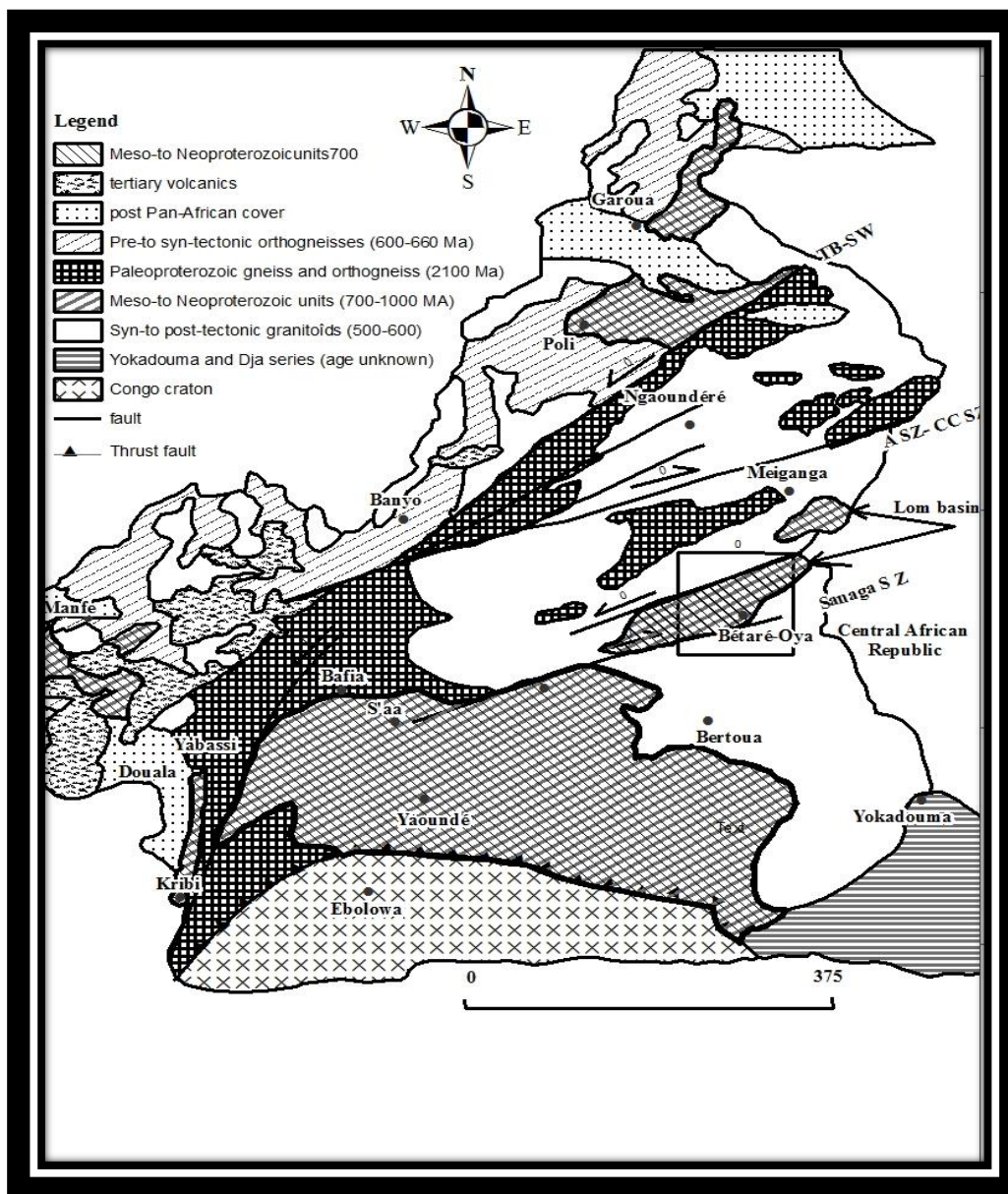
61 (b) A syn-collisional stage inducing crustal thickening and delamination of the subcrustal  
62 lithospheric mantle and comprising D1 and D2 deformations and S-type granitoids  
63 (640-610 Ma; Toteu et al., 2004);

64 (c) A post-collisional stage associated with D3 deformation (nappe and wrench)  
65 concomitant with exhumation of granulites, development of D4 shear zones, and  
66 emplacement of late-tectonic calc-alkaline to sub-alkaline granitoids (600-570 Ma).

67 The Pan-African formations of Cameroon belong to the mobile zone of Central Africa (Bessoles  
68 et al., 1980), also known as the Oubanguide chain (Poidevin, 1985). It is attached to the East to  
69 Pan-African formations of the Mozambican belt of submeridian orientation. To the West, it  
70 extends to the North of Brazil by the Sergipe range. Two large dextral mylonitic shear zones,  
71 the Sanaga Fault (Dumont, 1986) and the Cameroon Center Shear Zone, cross Cameroon from  
72 northeast to southwest. These major shears belong to the Oubanguid setback zone (Rolin, 1995),  
73 which continually follows from the Gulf of Guinea to the Gulf of Aden (Cornacchia et al.,  
74 1983). Geologically, the Pan-African mobile chain is composed of granites, schists,  
75 micaschists, and migmatites (Poidevin, 1985).

76

77



78

79

80 **Figure 1.A** Geologic map of Cameroon, showing major lithotectonic units: ASZ, Adamaoua

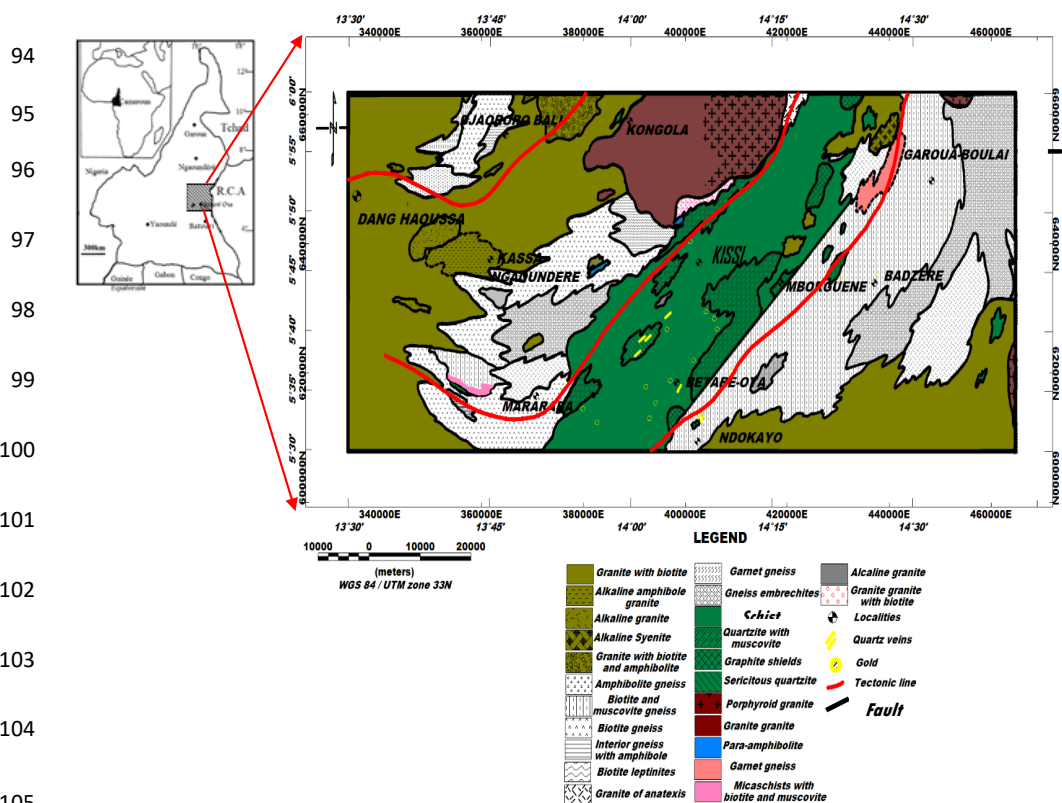
81 shear zone; CCSZ, Central Cameroon shear zone; TBSZ, Tcholliré- Banyo shear zone,



82 modified from Kankeu et al. (2009) as a document available in a public domain. The location  
 83 of the study area is marked by a box and shown in detail in Figure 1B.

84 **2.2. Local setting.**

85 The study area is located in eastern Cameroon; it is bounded by north latitudes 5°30'–6°, and  
 86 east longitudes 13°30'–14°45' (Fig. 1.B). The lithology comprises the Lom series constituted of  
 87 Neoproterozoic rocks sequence consisting of metasedimentary and metavolcanic rocks with  
 88 late granitic intrusions (Ngako et al., 2003). The lithologic units have a strong NE-SW regional  
 89 foliation deflected in places by the granitic pluton reflecting dextral and sinistral shear senses.  
 90 The rocks have been metamorphosed to greenschist facies and hydrothermal alteration  
 91 especially around the granitic plutons (Odey Omang et al., 2014). Gold is sporadically identified  
 92 in NE-SW quartz veins associated with early pyrite whereas a vug-filling late pyritization event  
 93 is barren (Asaah, 2010; Nih Fon et al., 2012).





106 **Figure 1.B** Geological map of the study area (Gazel and Gerard, 1954 modified as a document  
107 available in a public domain). In the center we have the Lom series marked by its greenschist  
108 facies. We can also perceive in red the tectonic lines that cross the study area.

109 The orography and hydrographic network would be structurally guided (Kouske, 2006), sub-  
110 divided into three major morphological units. The high altitude unit (800-1092 m) which is a  
111 vast peneplain enameled by interfluves with multiple vertices of alignment oriented NW-SE;  
112 N-S and NE-SW; The low altitude unit (652-760 m) which is a large flat-bottomed depression,  
113 in the center of which is a U-shaped valley, oriented NE-SW within which flows the Lom river  
114 and the intermediate unit (760-860 m) which corresponds to a long NE-SW oriented cliff  
115 connecting the high altitude unit to that of low altitude. In its northern part, this unit has an E-  
116 W orientation.

### 117 **2.3. Geophysical constraints**

118 Seismic anisotropy in Cameroon has been studied by Koch et al., (2012) through analysis of  
119 SKS splitting allows to identify four regions of distinct anisotropy: moderately strong NE-SW  
120 oriented fast polarization directions ( $\delta t \approx 1.0$  s) beneath two region: the Congo Craton in the  
121 south and the Garoua rift in the north; weak anisotropy ( $\delta t \approx 0.3$  s) between the Congo Craton  
122 and the CVL; N-S oriented fast polarization directions within the CVL, with  $\delta t \approx 0.7$  s. (Koch  
123 et al., 2012). Jean Benkhelil et al., (2002) used seismic data and proposed structural and  
124 chronostratigraphic scheme of the southern Cameroon basin (clayey sand, dolomitic to calcitic  
125 sandstone, marls and sandstone, dolomitic sandstone, granite, gneiss).

126 Gravity studies are carried out, Tadjou et al., (2004) identify many structures like contacts,  
127 dykes, fractures, and faults in the transition zone between the Congo Craton and the Pan-African  
128 Belt in Central Africa. Shandini et al., (2011) put into evidence in the northern margin of the  
129 Congo Craton a deep structure, which corresponds to a classical model of collision suture of  
130 the West-African Craton and Pan-African belt.



131 Owono et al., (2019) used 2.75D modelling of aeromagnetic data in Bertoua and shows  
132 intrusive bodies composed of gneiss and porphyroid granite and some domes with their roof  
133 situated at various depths not exceeding 1800 m from the surface. The structural map of the  
134 study area shows the trending of the structural features observed, namely, NE-SW, NW-SE,  
135 ENE-WSW, and WNW-ESE, respectively, while the E-W and N-S are secondary orientation  
136 of the observed tectonic evidence.

### 137 **3. Materials and Methods**

#### 138 ***3.1. Data acquisition and processing.***

139 The aeromagnetic data were collected in Cameroon by Survair Limited through the  
140 Cameroon/Canada cooperation framework in the 1970s. Data were collected along N-S flight  
141 lines at 750 meters spacing, with a flying height of 235 meters; the measurements involved a  
142 magnetometer with a sensitivity of 0.5 nT (Paterson et al., 1976). Aeromagnetic anomalies map  
143 has been digitized using the geographical information system software (Mapinfo Pro. 16.0) and  
144 interpolated on a 850 m cell-sized grid. The estimate error introduced is 0.28 mm which is  
145 usually considered to be distinctive capacity of human vision (Achilleos, 2010). Gridding and  
146 processing were done with Geosoft v8.4 software. The IGRF-84 reference field values were  
147 removed from the observed magnetic data.

#### 148 ***3.2. Methods***

##### 149 ***3.2.1. Upward continuation theory.***

150 The upward continuation subjects the observed potential field on a surface, in order to obtain  
151 the field which would be observed on another surface above of the initial surface of observation.  
152 In this study it helps us to easily visualize the effects of the deep sources and to remove the  
153 regional effect. This method was described by (Blakely, 1996).

##### 154 ***3.2.2. The Tilt-angle approach.***

155 The tilt-angle (Miller and Singh 1994; Verduzco et al., 2004; Salem et al., 2007) is defined  
156 by the equation (1) below for a potential field anomaly T:





157 
$$\theta = \tan^{-1} \frac{\frac{\partial T}{\partial z}}{\frac{\partial T}{\partial h}} \quad (1) \quad \text{where}$$

158  $\frac{\partial T}{\partial h} = [(\frac{\partial T}{\partial x})^2 + (\frac{\partial T}{\partial y})^2]^{1/2}$  is the horizontal gradient magnitude and  $\frac{\partial T}{\partial z}$  is the vertical gradient;

159  $\frac{\partial T}{\partial x}$ ,  $\frac{\partial T}{\partial y}$  are respectively the horizontal gradients along the x and y directions.

160 In 2007, Salem et al., extended the method to the determination of depth to source by relating  
161 the depth  $Z_c$  of the source and its horizontal location  $h$  to the tilt-angle through equation (2):

162 
$$\theta = \tan^{-1} \left( \frac{h}{Z_c} \right) \quad (2)$$

163 This means that the contacts are located for a nil tilt ( $h = 0$ ) and the depth corresponds to  
164 horizontal distance between  $0^\circ$  and  $\pm 45^\circ$  contours, i.e.  $h = \pm Z_c$  (Salem et al., 2007).

### 165 3.2.3. Qualitative analysis by Tilt-angle derivative.

166 The tilt angle operator can be used for mapping geological structures because it permits to  
167 locate and to delimit their contacts and their shapes (Miller and Singh, 1994). By coupling it to  
168 the extension upward, it becomes more interesting because one obtains the lateral extension of  
169 body but also in depth therefore its three-dimensional shape.

### 170 3.2.4. Euler's Deconvolution.

171 This method was introduced by Thompson, (1982) based on the Euler's homogeneity  
172 equation to solve for the source depths for profile data. Reid et al., (1990) extended the operator  
173 to gridded data by using equation (3): w

174 
$$\frac{(x-x_0)\partial M}{\partial x} + \frac{(y-y_0)\partial M}{\partial y} + \frac{(z-z_0)\partial M}{\partial z} = N(B-M) \quad (3)$$

175 where  $(x, y, z)$  represent the coordinates of the observation point,  $(x_0, y_0, z_0)$  the coordinate of  
176 the magnetic source,  $M$  and  $B$  are the field at the observation point and regional the field  
177 respectively; and  $N$ , the structural index, characterizes the variation rate of the field in relation





178 to the distance due to the type of source (table 1.A). In this study, we take the advantage of the  
179 clustering in depth to define the correct structural index.

180 **Table 1.A** Structural index for magnetic sources of different geometries.

Source	Smellie model	Structural index
Sphere	Dipole	3
Vertical line end (pipe)	Pole	2
Horizontal line (cylinder)	Line of dipoles	2
Thin bed fault	Line of dipoles	2
Thin sheet edge	Line poles	1

181

### 182 **3.2.5. 2.75D modeling.**

183 A very useful variation on the 2D model which removes the restriction of infinite strike  
184 length, and is easier to define than the more complex 3D model, is a model with constant cross-  
185 section extending over a finite strike length. This is known as 2.5D model. When the source  
186 can have different strike extents on either side of the modelled profile, or the strike or plunge  
187 of the body is not perpendicular to the profile, this is called a 2.75D model.

188 The 2.75D model represents the subsurface as a series of polygonal prisms with horizontal  
189 axes (X) and finite extent in the strike direction (Y). This method was described by Skalbeck et  
190 al., (2005). Geologic models were constructed with GM-SYS operator of Geosoft using the  
191 2.75D modelling algorithm from Won and Bevis (1987), based on the analyses of Rasmussen  
192 and Pedersen (1979). The 2.75D model gives the interpreter control of the third dimension  
193 without the complexity of defining and manipulating a full 3D model.

## 194 **4. Results**

195 After interpolation, data have been reduced to the equator using the Fourier transform  
196 (Inclination  $I = -11.98$  deg, Declination  $D = -4.96$  deg) on January 1, 1970. This transformation



197 eliminated the tilt of the earth magnetic field due to inclination and positioned anomalies  
198 directly above the corresponding magnetic source.

199 ***4. 1. Interpretation of the aeromagnetic total field reduced to Equator.***

200 The magnetic field over the Bétaré-Oya area has a complex magnetic pattern (Fig. 2.A). For  
201 better characterization of the geological structures, we subdivided the area into different units:

202 *Unit A*

203 The major observable singularity is in the center where a large positive anomaly about 5 km  
204 wide and up to 100 nT is observed. It is oriented NE-SW along the major tectonic feature in  
205 this area, namely the tectonic line of the Sanaga (Fig. 1.A). Comparing with the geological map  
206 in Figure 2, this signal is mainly due to volcano-clastic schists (with gold deposit) also called  
207 Lom schists associated with conglomeratic quartzites with intrusions of granitoids (Kankeu et  
208 al., 2009). Hence, the presence of the anomalies with similar signatures could be related the  
209 circulation of hydrothermal fluids rich in magnetic minerals along the Betaré-Oya Shear Zone  
210 (BOSZ).

211 *Unit B-C*

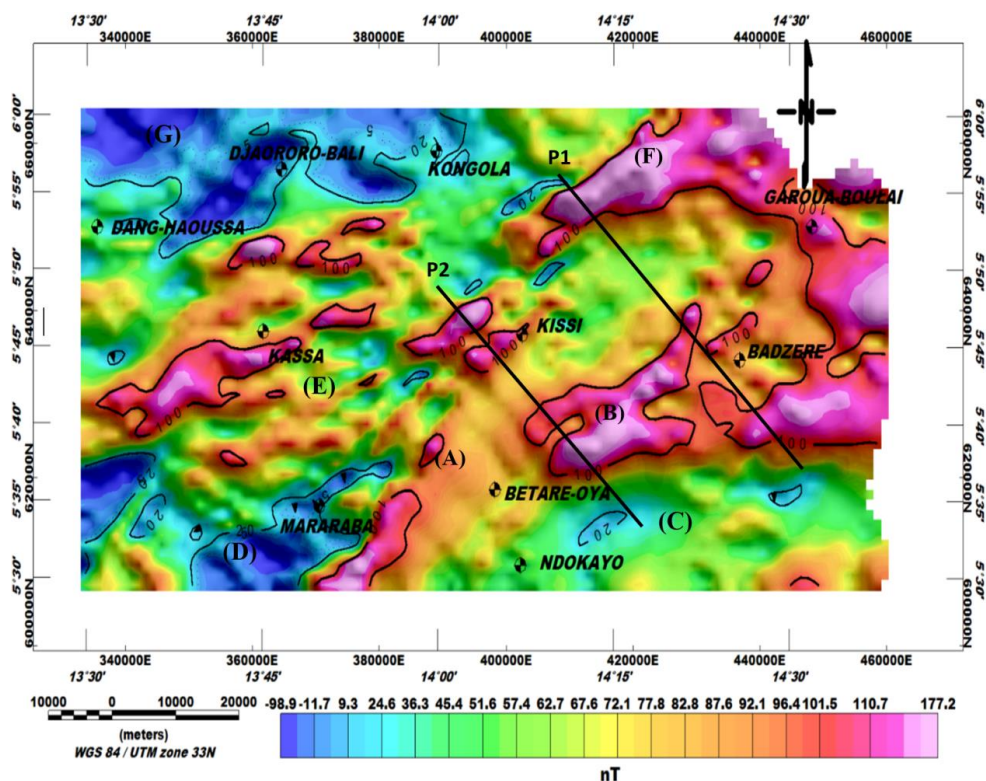
212 In the northeastern part of Bétaré-Oya, particularly around Badzéré, two positive and  
213 heterogeneous bipolar anomalies are observed. The positive pole is slightly more developed  
214 than the negative pole located in the south of the area at Ndokayo, with very long wavelength  
215 of about 22 km. Its amplitude is quite high and reaches 120 nT. It is aligned with the one of the  
216 major foliations in this area trending E-W. The shape and amplitude of these anomalies suggest  
217 high susceptibilities of the causative bodies, such as igneous granitoids known in this area.

218 *Unit D-E*

219 In Mararaba and Kassa, there is a large magnetic anomaly with a bipolar shape, whose positive  
220 pole labeled as E in Figure 3 and the negative pole D. It is characterized by a long wavelength  
221 with variable amplitude reaching 150 nT, its approximate direction is ENE-WSW. We can also



222 observe positive and negative anomalies of intensity 100 nT and 20 nT, elongated shapes,  
223 circular and semi-circular, short wavelength-oriented ENE-WSW, NW-SE, NE-SW  
224 corresponding to structural directions in the study area (Kankeu et al., 2009, Nih Fon et al.,  
225 2012).



226

227

228 **Figure 2.A** Total magnetic intensity (TMI) map reduced to the equator.

229 *Unit F*

230 In the northwestern part of Garoua-Boulai, a positive and heterogeneous anomaly with irregular  
231 shapes, normal polarity and a very long wavelength of about 22 km has been observed. Its  
232 amplitude is quite high and reaches 177 nT. Its approximate direction is ENE-WSW. It is



233 probably associated with the meta-volcanic outcrops of the meta-lava within the schistous Lom  
 234 series (Regnault, 1986).

235 *Unit G*

236 The lowest magnetic intensities are recorded in the north-west near Djaororo-Bali, where  
 237 negative anomalies with amplitudes down to -98.9 nT are found associated with surface meta-  
 238 sediments such as modified-biotite gneiss overlying the old metamorphic basement.

239 **4. 2. Tilt-angle on residual map.**

240  
 241 The residual map is obtained by subtracting the total magnetic field map reduced to the equator  
 242 to the regional map. The determination of the optimum regional anomaly map for the study area  
 243 lies on the method of Zeng, (1989). This method consists in determining a suitable altitude for  
 244 upward continuation in the study area. The extrema of each altitude of upward continuation are  
 245 then counted (table 1.B). These are points where the gradient is null. Further, a graph of extrema  
 246 versus altitudes of upward continuation is plotted (Fig. 2.B). Finally, the suitable altitude (h=10  
 247 km) necessary for the upward continuation technique is determined graphically.

248

249 **Table 1.B** Maxima and altitudes of upward continuation.

Number of maxima	Altitudes of upward continuation (Km)
38	0
19	1
14	2
6	3
5	4
5	5
2	6
1	7
1	8

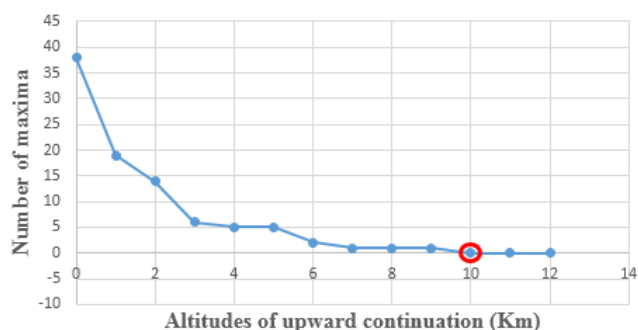
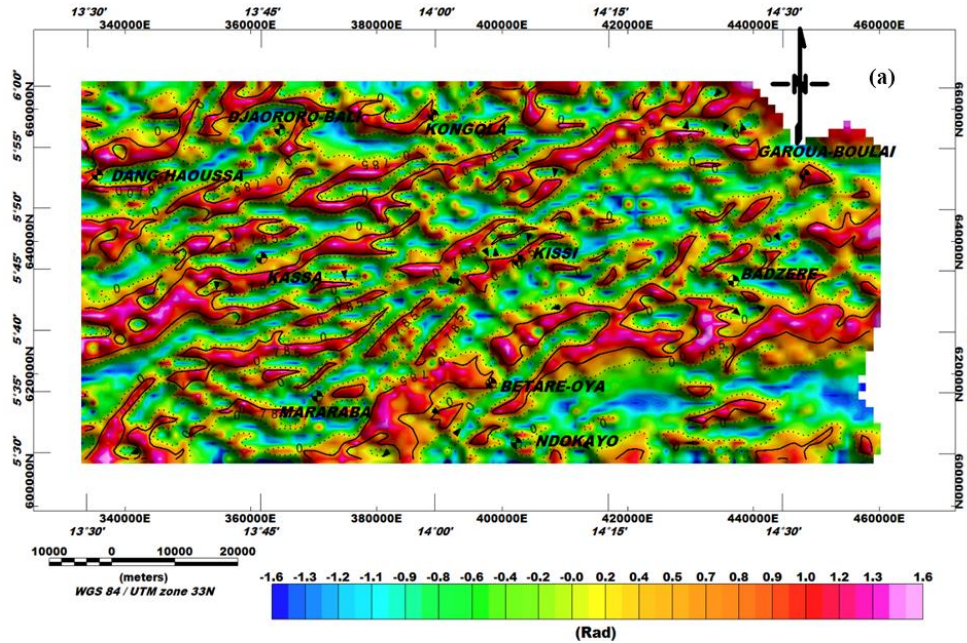


**Figure 2.B** Number of extrema versus upward continuation height. From h = 10 km (circle in red), the number of maxima becomes constant and does not vary anymore.



1	9
0	10

250  
 251



252

253 **Figure 2.C** Tilt angle on residual map.

254 The generated tilt-angle's map (Fig. 2.C) represents possible lineaments of the study area.  
 255 On this map it can clearly be seen that the signal is uniformly distributed in -1,6 rad to 1,6 rad  
 256 intervals; thus, making it possible to map the lineaments with a very high resolution. The  
 257 presence of several accidents marks the heterogeneity of the basement in this area as well as  
 258 the intense deformation undergone by its subsurface. The lineaments and spatial patterns of  
 259 geophysical attributes are important information that can be obtained from magnetic  
 260 interpretations. Steep features and straight faults are commonly expressed as subtle lineaments  
 261 of potential field. This expression can be gradient zones, local anomaly alignments of different  
 262 types and shapes, aligned breaks, or discontinuities in the anomaly model.

263

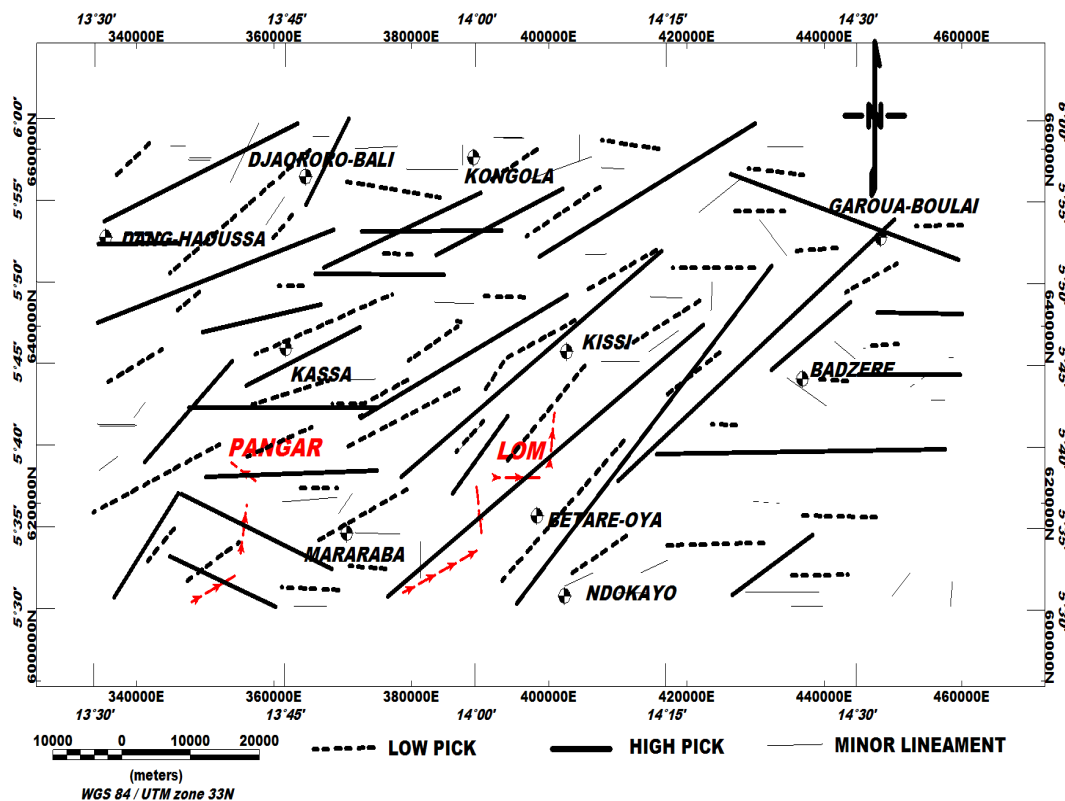
264



265

266 **4.3. Structural map.**

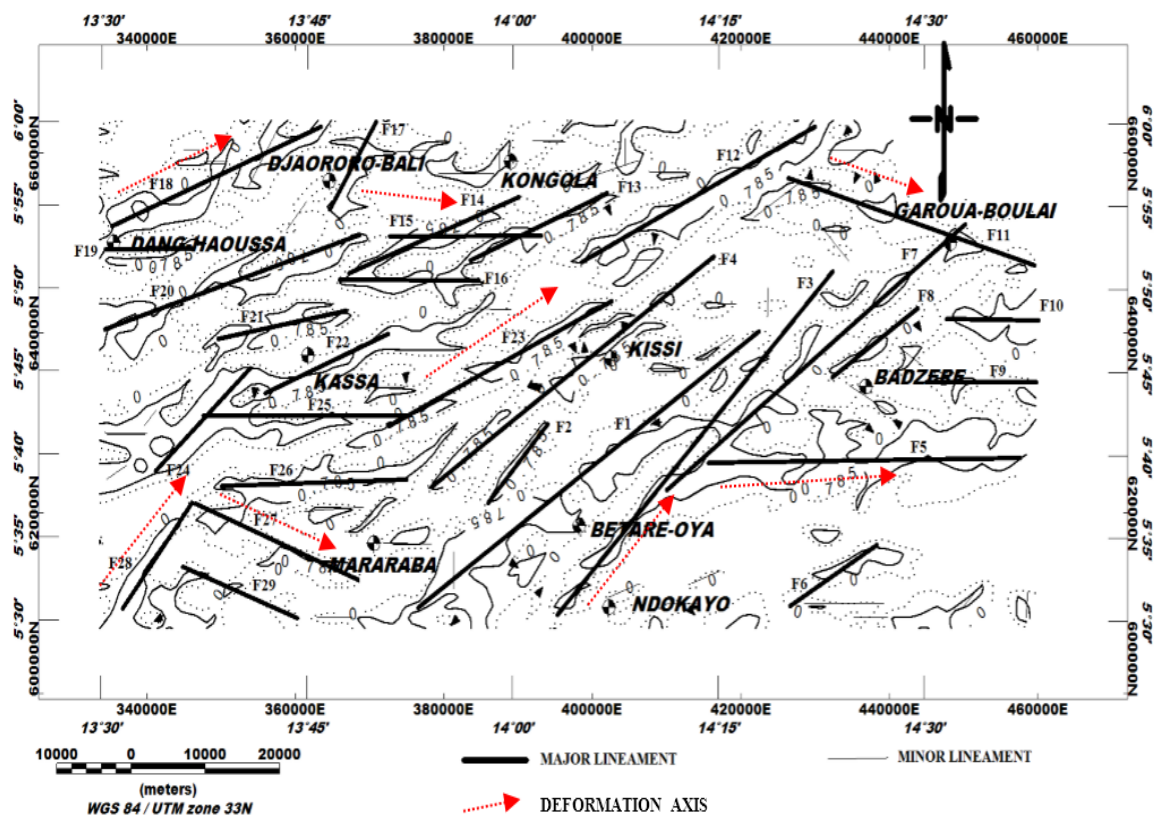
267 To characterize information, we were interested in the peaks of anomalies derived from tilt  
268 angle derivative (Fig. 2.C). We counted 111 lineaments among which: 45 have lengths varying  
269 between (2.5 - 10.8) km; 37 minor lineaments varying between (1.2 - 2.3) km and 29 major  
270 lineaments between (2.4 - 15.6) km. Five structural families NE-SW are observed; ENE-WSW;  
271 E-W; NW-SE; N-S, the major structural direction being NE-SW (Fig. 3.A).



272

273 **Figure 3.A** Structural map of the study area.





274

275 **Figure 3.B** Major faults map superimposed on tilt-angle contours. On this map we observe  
276 the major regional deformation axes (NE-SW, E-W, ENE-WSW and NW-SE) as well as the  
277 associated faults (F1 to F29).

278

279 The longest faults are present at the eastern edge of the Lom series with lengths of more  
280 than 15 km (F1, F3, F7). To the west we also note the NE-SW F4 fault with more than 10 km  
281 length which marks the limit of the Lom series (Fig. 3.B). The most remarkable is the change  
282 of direction of compression or deformation axes. The E-W events marked by the faults F15,  
283 F16, F19, F25, F26 at the eastern edge of the Lom and by the faults F5, F9, F10 in the west,  
284 seem to have been taken up by the tectonic accidents F1, F2, F3, F4, F7, F8, F12, F23  
285 punctuated by the Betaré-oya shear zone (BOSZ). The same phenomenon occurs in the extreme  
286 west of the study area around Dang Haoussa and Mararaba with the ENE-WSW (F13, F14,

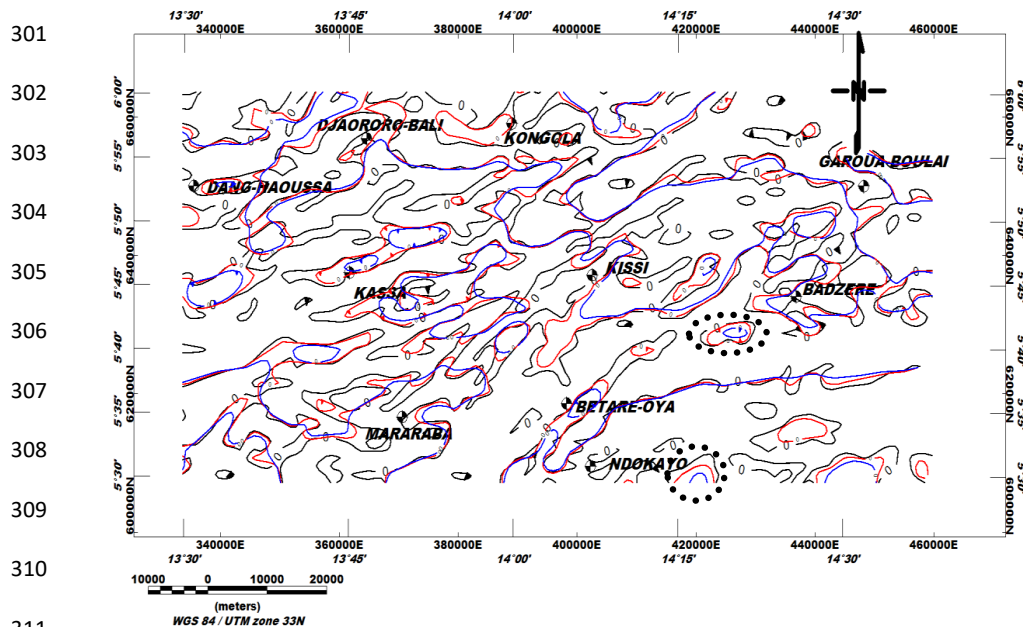




287 F18, F20, F21, F22) and NW-SE (F27, F29) accidents, respectively. These discrepancies  
288 suggest the passage of shear faults. The curvature (type II) structures corresponding to foliations  
289 induce most of the major fault network present in the Bétaré-oya area. In order to confirm the  
290 results obtained by the tilt-derivative, we apply the Euler Deconvolution method.

#### 291 4.4. 3D extension of anomalies.

292 By superposing the zero contours of tilt-angle of the residual map, we obtain Figure 3.C  
293 which no perfect superimposition of sources on the previous ones, hence assuming the  
294 heterogeneity of the basement and existence of movements that affected the subsurface  
295 formations. Deep crustal tightening of volcano – clastic rocks in the vicinity of Betaré - Oya  
296 confirms that the site is affected by shear tectonics (Soba, 1989), causing deep and shallow  
297 faults. This is witnessed by the contact between the granito-gneissic rocks and the Lom schists  
298 (Fig. 1.B). These contours delimit the edges of the magnetic source, so their superposition in  
299 depth allows to have an idea about the disposition, the extent, the dip and the shape of the  
300 geological sources responsible for the magnetic anomalies observed.





313 **Figure 3.C** Superposition of contours ( $\Theta=0^\circ$ ) of Tilt angle of RTE upward continued to 1 km  
314 (red) and 2 km (blue).

315 East of Ndokayo, Kassa and south-east of Mborguene, several structures lose extension in  
316 depth, taking the form of a basic cone of revolution located on the surface (interrupted circle).

317 The presence of this regional-scale fold system, which controls all movements in the area  
318 (BOSZ), suggests an interconnection of crustal geological structures by lines of faults and  
319 foliations. Hence the structural elements highlighted in this study (folds, faults, dykes, etc.)  
320 globally belong to Pan-African tectonics.

#### 321 **4.5. Quantitative analysis**

##### 322 **4.5.1. Tilt-angle.**

323 The tilt-angle operator makes it easy to determine the depth of the vertical contacts (Salem  
324 et al., 2007) by estimating the distance between the zero-angle contours and those  
325 corresponding to the values  $\pm 45^\circ$  (Fig. 3.B). We have determined the average depths interval  
326 ranges from 1 to 3 kilometers for major lineaments (Table 1.C).

##### 327 **4.5.2. Euler deconvolution.**

328 Euler's solutions allowed us to verify the position of the contacts obtained by the tilt angle  
329 method as well as their depth.

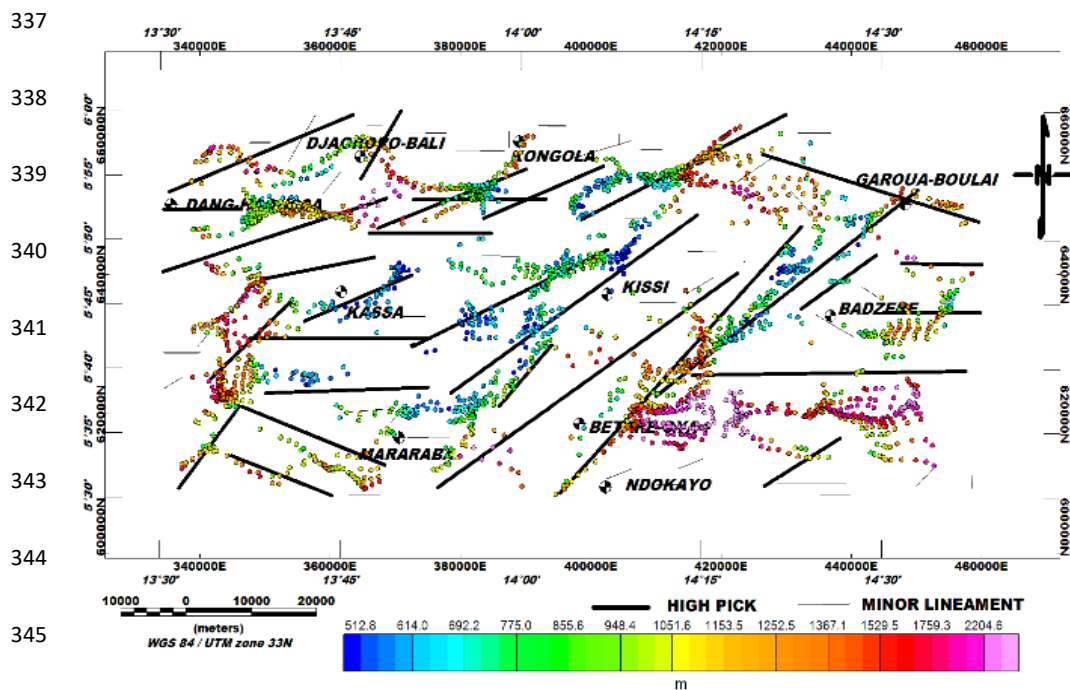
330 The superposition of the structural map with Euler's solutions allowed us to delimit deep and  
331 superficial faults, dykes and veins; to delineate tectonic lines established by previous geological  
332 studies (Gazel et al., 1954) and to compare with results from the tilt angle method (Fig. 4.B).

333

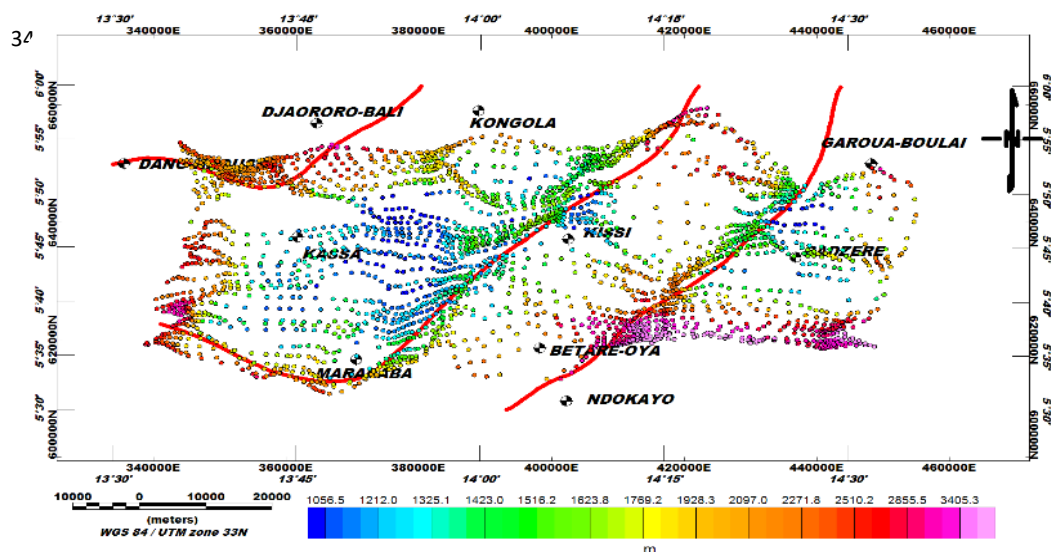
334

335

336



347 **Figure 4.A** Euler solution (N=1; W=25; Z=10%).



356 **Figure 4.B** Euler solution (N=2; W=20; Z=10%). The Euler maps above allow for a  
357 comparative study with the results obtained from the tilt derivative. They also make it possible



358 to confirm the tectonic lines of the zone (in red) highlighted in the work of Gazel and Gerard,  
 359 (1954) and to estimate their depths.

360 On Euler's solutions map we have perfectly distinguished the limits of the intrusive bodies  
 361 and the deeper faults. On these maps, we observe five main directions of structures namely:  
 362 NE-SW; ENE-WSW; E-W; NW-SE; N-S (Fig. 3.B). In addition, the vertical contacts are  
 363 clearly visible on Euler solutions map and extend over 15 km length.

364 The deepest accidents are mainly NE-SW to E-W with depths of over 3500 m and are well  
 365 located at the eastern limits in the Lom series and the Badzéré gneisses contact zone and also  
 366 around the East fault of Bétaré-oya. In the south-west of the map, at Mararaba, Euler's solutions  
 367 allow to detect approximately NW-SE faults that was the result of the highlighted tectonic line  
 368 (Fig. 4.A) and whose depths are estimated at 3000 m. We obtain depths ranging from 0.5 to 3.6  
 369 km. Figure 4.B clearly shows tectonic directions which dominate all subsurface movements of  
 370 the study area and their depths ranging from 1 to 3.4 km.

371 **Table 1.C** Main faults of Lom series. This summary table is obtained after comparing the  
 372 results from the Euler deconvolution method and the tilt derivative.

373

Faults	Directions	Dips	Depths (km)
F1	N56°E	Vertical	3,6
F2	N44°E	NW	2,1
F3	N44°E	NE	2,9
F4	N56°E	Vertical	1,3
F5	N90°E	Vertical	2,6

F6	N60°E	NE	2,1
F7	N56°E	Vertical	2,9
F8	N56°E	Vertical	1,6
F9	N90°E	Vertical	2,3
F10	N90°E	Nord	3,5
F11	N107°E	NW	2,6
F12	N65°E	NW	3,5



F13	N65°E	Vertical	1,5
F14	N70°E	Vertical	2,5
F15	N90°E	Nord	2,3
F16	N90°E	Nord	1,2
F17	N32°E	Vertical	2,3
F18	N70°E	Vertical	2,6
F19	N90°E	NW	2,6
F20	N70°E	Vertical	3,6
F21	N80°E	NW	3,6

F22	N65°E	Vertical	1,5
F23	N65°E	Vertical	2,3
F24	N47°E	Vertical	3,6
F25	N90°E	Vertical	3,5
F26	N90°E	Vertical	1,3
F27	N110°E	Vertical	2,3
F28	N40°E	Vertical	2,3
F29	N110°E	Vertical	2,5

374

375

376 **4.5.3. 2.75D modeling.**

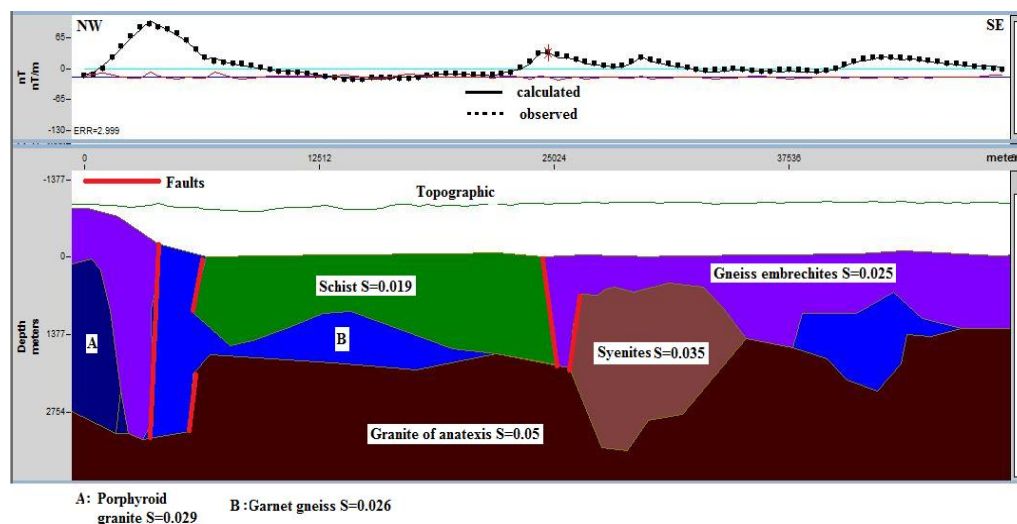
377 **Profile 1**

378 This profile extends 48.8 km NW-SE through Badzere and Mborguene. It crosses 6 geological  
 379 formations from NW to SE, namely: porphyroid granite, granite with biotite, Gneiss  
 380 embrechites, granite of anatexis, schists, biotite and muscovite gneiss (Fig. 2.A). The strongest  
 381 anomalies are localized in the NW of the profile with an intensity of 177 nT. The basement  
 382 obtained is made up of granites anataxis which are old magmatic rocks forming the old  
 383 basement complex and put in place during the first half of the Precambrian. Its maximum depth  
 384 is  $h = 3.608$  km which agrees with the depths obtained by the Euler convolution (Fig. 5.A). Its  
 385 susceptibility is  $S = 0.05$  SI. Above, one can observe the embrechite gneisses ( $S = 0.025$  SI),  
 386 volcano-clastics schists ( $S = 0.019$  SI). This contact between the granito-gneissic rocks and the  
 387 Lom schists has therefore caused several fractures and faults, represented here by several  
 388 intrusions: porphyroid granite ( $S=0.029$  SI), garnet gneiss ( $S = 0.026$  SI), syenites ( $S=0.035$



389 SI). Our model agrees with previous geological (Poidevin, 1985; Gazel and Gerard, 1954;  
390 Kouske, 2006; Ngako et al., 2003) and geophysical studies (Koch et al., 2012; Owono et al.,  
391 2019). These intrusions were set up during the pan-African orogenesis (Eno Belinga, 1984) and  
392 are present in our geological map (Fig. 1.B).

393



394

**Figure 5.A** 2.75D model obtained from profile P1.

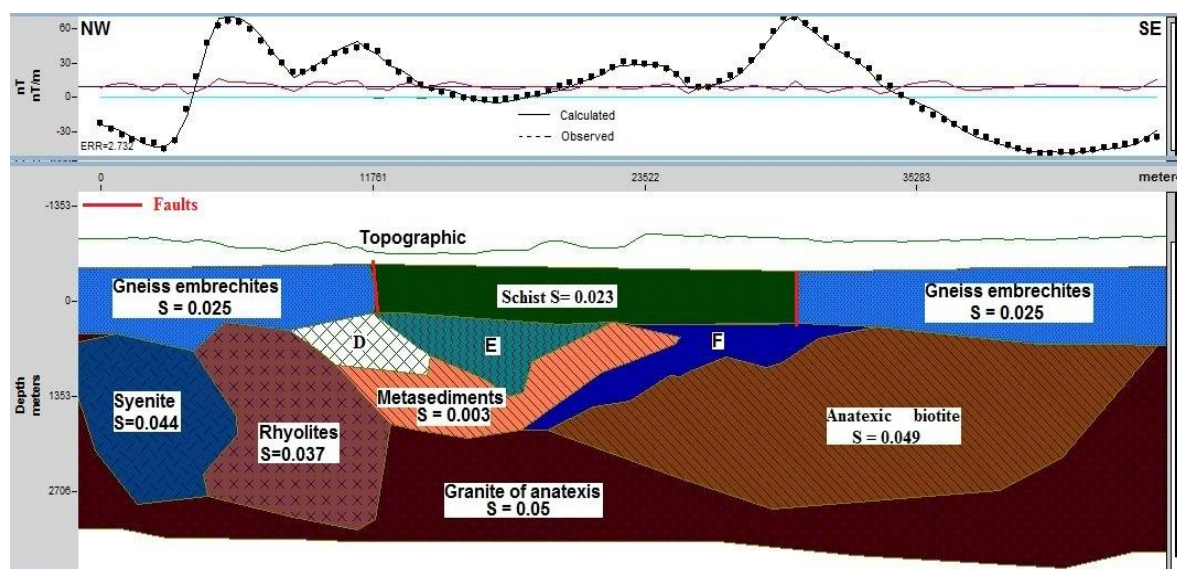
## 395 Profile 2

396 The profile 2 extends 46 km along the NW-SE direction through Bétaré-oya and Kissi. It crosses  
397 5 geological formations: Biotite leptinites gneiss, quartzite with muscovite schists, schists,  
398 biotite and muscovite gneiss, alkaline granite (Fig. 2.A). The lowest anomalies are localized in  
399 the NW of the profile with an intensity of -43.4 nT, while the strongest are on the edge of the  
400 Lom schists with a maximum value of 65.6 nT. The obtain basement is made up of anatexite  
401 granites ( $S = 0.05$  SI), intruded by strongly magnetized rocks such as syenite ( $S = 0.044$  SI),  
402 rhyolite ( $S = 0.037$  SI) and anatexic biotites ( $S = 0.048$  SI). Upstream, one can note the  
403 embrechite gneisses ( $S = 0.025$  SI) discordant to volcano-clastics schists ( $S = 0.023$  SI) located  
404 above the metasediments rocks ( $S = 0.003$  SI). One can also observe several intrusions  
405 micaschists ( $S=0.0186$  SI), Graphite ( $S=0.00012$  SI) and Garnet gneiss ( $S=0.027$  SI). The



406 geological layers obtained are located below the topography and the maximum depth is  $h =$   
407 3.419 km (Fig. 5.B), in agreement with the data resulting from the Euler deconvolution. The  
408 model from this profile is in accordance with previous studies (geology, seismic, magnetic etc.).  
409 We note intrusions from the pan-African orogenesis (Poidevin, 1985; Gazel and Gerard, 1954;  
410 Kouske, 2006; Ngako et al., 2003; Koch et al., 2012; Owono et al., 2019; Eno Belinga, 1984),  
411 located in our geological map (Fig. 1.B).

412



**Intrusive bodies**

**D** : Micaschists  $S=0.0186$

**E** : Graphite  $S=0.00012$

**F** : Garnet gneiss  $S=0.027$

413 **Figure 5.B** 2.75D model obtained from profile P2.

414 **5. Regional analysis of the 2.75D models**

415 The geological synthesis of Cameroon allows us to have a lithostratigraphic sketch of the  
416 Lom Formation. Recently, the near-surface work Mboudou et al., (2017) at Betare-Oya  
417 proposes the lithological model with top soil, saprolites, sandy layer, conglomeritic sand and  
418 schist formations.

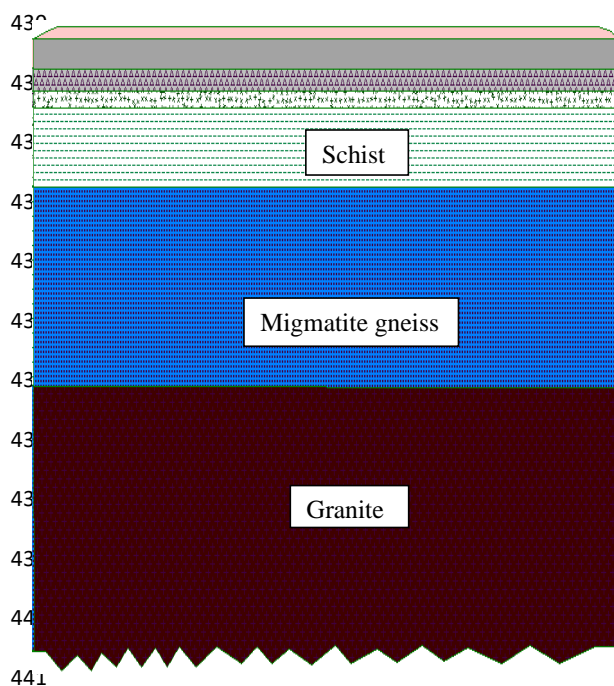
419 On our model from profile 2 that passes through the locality of Bétaré oya, we observe that  
420 the first layers of rocks encountered are well below the topography that is explained by the fact





421 that the method used allows us to highlight the structuring of deep formations. This would have  
 422 the effect of hiding the superficial (sediments) hence the observed shift. Thus, the first  
 423 formation detected on our models at Betare-Oya is schist. We can therefore complete this  
 424 lithological model with the formations of the pan-African basement highlighted by our  
 425 geophysical methods (Fig. 5.C) and propose the litho-stratigraphic model updated below (table  
 426 2). Crustal formations in our model are in accordance with those obtained by Jean Benkhelil et  
 427 al., (2002) from seismic data south Cameroon and summary above and geological study of  
 428 Mboudou et al., (2017).

429



Rocks	Thicknesses (m)
Top soil	< 1,5
Saprolites	2
Sandy layer	1,5
Conglomeritic sand	1,4
Schist	227, 18
Migmatite gneiss	699,83
Granites	> 1600

**Table 2** Nature of formations.

442

443 **Figure 5.C** Improve sketch of lithologic profile of Betare Oya basin. The scale map is 2/1000.

444 This model confirms the granite-gneiss nature of the pan-African base.

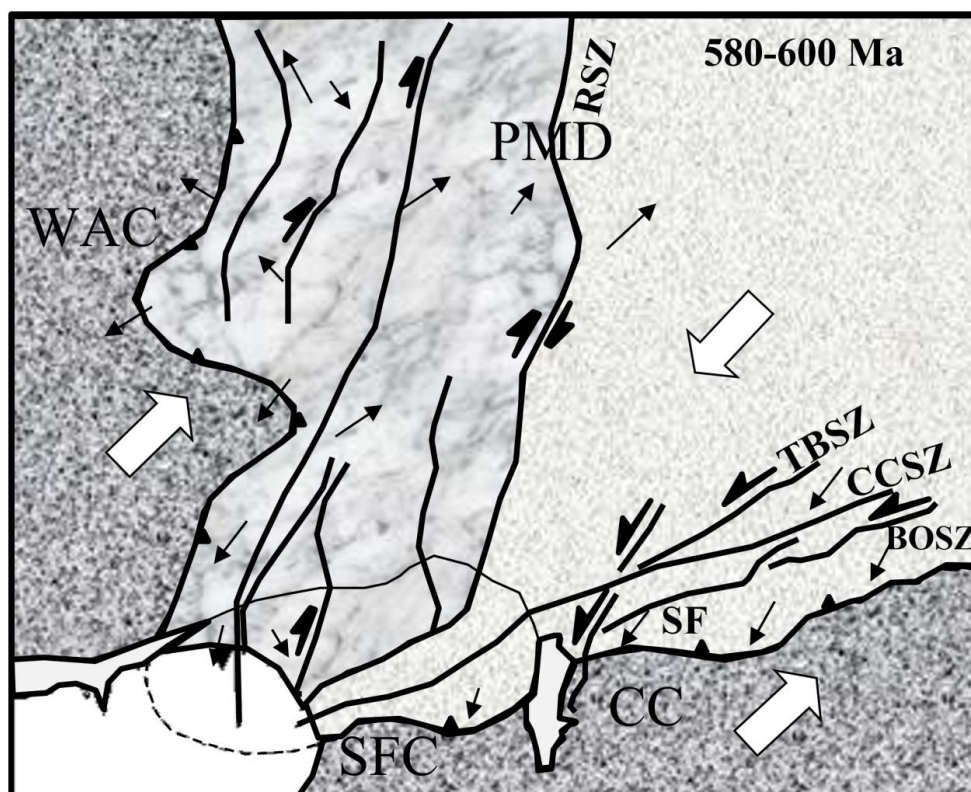
445 The major faults highlighted in this work controlled by the Betare - Oya shear zone (BOSZ)

446 belong in fact to a wider network of faults found on the Pan-African and which would extend

447 to the São Francisco Craton (SFC) by the central Cameroon shear zone (CCSZ). Indeed, the



448 work of Toteu et al., (2004) suggests that the Reghane shear zone, which during the whole Pan-  
449 African evolution (650-580 Ma) only recorded dextral wrench movement, can be considered as  
450 a major boundary separating mobile domain in two (Fig. 5.D) - a western part where the  
451 tectonics is controlled by the motion of the WAC and an eastern part controlled by the motion  
452 of the Congo craton.



453

454 **Figure 5.D** The Pan-African mobile domain (PMD) between the West Africa craton (WAC)  
455 and the São Francisco (SFC) and Congo (CC) cratons showing two sub-domains, west and east,  
456 separated by the Raghane Shear Zone (R.S.Z.). Horizontal lines represent the Tcholliré-Banyo  
457 shear zone (T.B.S.Z); central Cameroon shear zone (C.C.S.Z); Sanaga fault (SF); Betare-Oya  
458 shear zone (BOSZ). Small arrows correspond to stretching lineations and large arrows to  
459 movement directions of blocks during D3 (600-580 Ma). Toteu et al., (2004) modified (initial  
460 document is available in a public domain).  
461

## 462 6. Discussion

463 The structural map obtained (Figure 3.A) shows a great disparity in the distribution of  
464 lineaments which can be explained in part by the general tectonics of the area. Hence, the



465 collision between the stable Archean craton in the South and one of the two Paleoproterozoic  
466 blocks in the north during the Pan-African orogeny 700 Ma, would have caused a flattening of  
467 the basement and intrusions in the old Precambrian basement, causing the major NE-SW  
468 oriented lineaments related to the Lom schists. According to the Cameroon geological  
469 synthesis, these intrusions are identified as granitic batholiths placed during regional  
470 deformation D1 and D2.

471 On both sides of the Lom series, there are major NE-SW lineaments representing the  
472 bounding faults of the Lom series with the granite-gneiss rocks. The E-W; NE-SW and N-S  
473 lineaments may represent major tectonic structures marking the change in the structural  
474 direction between the trans-Saharan (N-S) and the Oubanguides (E-W) chains.

475 At the local scale, the deformation D2 is characterized by L2 lineations representing here  
476 stretches of quartz minerals-oriented E-W. The ENE-WSW oriented lineaments appear to  
477 correlate with the mylonitic deformations occurring during the D3 phase while the ones  
478 trending NW-SE related to senestral and dextral recesses and represent fractures with or without  
479 lode flow. These structures much more abundant near Mararaba and could be the target for  
480 future mining studies.

481 The geoelectrical study of Nih Fon et al. (2012) in our study area identified NE-SW  
482 oriented irregular anomaly zones. These correlate with the quartz veins known in the region  
483 and are aligned with the regional shear zone. The morphological units identified also present  
484 NW-SE, N-S, NE-SW and E-W directions. In addition, Kouske (2006) reveals that the  
485 hydrographic network of the study area has two major directions, NE-SW and NW-SE and it is  
486 dense and dendritic type.

487 The P1 and P2 models obtained can be used as pseudo 3D imagery of the Lom basement.  
488 Previous geological studies indicate that the area was a subject to intense metamorphic activity  
489 during Neoproterozoic that has resulted in schist formation (Coyne et al., 2010). The contact  
490 between this schistous series and the gneissic and granitic rocks of the basement resulted in



491 multiple fractures and faults (Gazel et al., 1954; Soba, 1989). The litho-stratigraphic sketch  
492 proposed by our models derived from the magnetic profiles and work of Mboudou et al., (2017)  
493 are consistent with previous geological work that asserts that the Pan-African basement would  
494 be made up of migmatites and granitic to ortho-gneissic and biotite rich rocks (Poidevin, 1985;  
495 Gazel and Gerard, 1954; Kouske, 2006; Ngako et al., 2003; Koch et al., 2012; Owono et al.,  
496 2019; Eno Belinga, 1984).

497 From the mining point of view, the artisanal gold indices are places located near the  
498 Lom and Pangar rivers (Nih Fon et al., 2012). These alluviums correlate with NE-SW trends in  
499 our structural map. Since the structures in our study area are structurally guided, it can be  
500 concluded that the alluvial deposits observed and exploited by residents are some signs that  
501 have been leached and transported by the waterways. Overall, the geological structures obtained  
502 from the data processing correspond to the ductile-brittle structures such as shear zone and  
503 faults. These structures constitute pathway for both mineralizing fluids and ground water. Since  
504 several gold mines exist in Betare-Oya area, the new mapping approach could be an important  
505 guide for the identification of the structures that control the gold mineralization in the area.

## 506 **7. Conclusion**

507 In this work, some new analysis techniques were applied on aeromagnetic data to delineate the  
508 sub-surface structures. The results obtained highlight the axes of compression, folding and  
509 shearing; mylonitic veins (veins are at the outcrop's scale) several kilometers long and oriented  
510 NE-SW. The regional and local structural settings of the area are characterized by major faults  
511 and other structural elements mainly striking in the NE-SW, NW-SE, ENE-WSW, N-S and E-  
512 W directions. Major trend in the NE-SW direction represents the dominant tectonic trend which  
513 is the prolongation of the Central Cameroon Shear Zone (CCSZ) in the study area. Several folds  
514 and faults evidenced by this study correlate with past studies while others are inferences. The  
515 depths of major accidents in the area have been estimated between 1.2 to 3.6 km and the NE-  
516 SW structures on our structural map are proposed here for a possible gold exploration. The



517 models from the P1 and P2 profiles have enabled: to propose a structuration of the superficial  
518 crust of the Lom highlight the main rocks and intrusions responsible of the observed anomalies  
519 (porphyroid granite, garnet gneiss, syenites, micaschists, Graphite and Garnet gneiss), identify  
520 deep and shallow fractures, their depths and to propose a lithostratigraphic model in agreement  
521 with the previous works. Finally, we note that the tilt angle coupled to the upward continuation  
522 is an interesting tool for 3.D modeling.

### 523 **Data Availability**

524 The data used to support the findings of this study are available from the corresponding  
525 author upon request.

### 526 **Author Contribution**

527 Christian Emile Nyaban performed the data analyses, modelling and preliminary interpretation  
528 including preparation of the manuscript in conjunction with all the co-authors; Theophile  
529 Ndougsa-Mbarga design the topic, gives the orientations for the investigation and reviewed the  
530 quality of the models and related interpretation and the entire manuscript ; Marcelin Bikoro-  
531 Bi-Alou defines the criteria and the physical parameters for the 2D3/4 modelling with the first  
532 author; Stella Amina Manekeng-Tadjouteu and Stephane Patrick Assembe have worked on the  
533 review of quality and quantitative analyses of respectively maps and 2D3/4 models.

### 534 **Competing Interest**

535 The authors declare that there are no conflicts of interest regarding the publication of this paper.

### 536 **Acknowledgements**

537 The authors thank the reviewers for their valuable comments.

### 538 **References**

539 Achilleos, G. A., 2010. Approaching a model for estimating horizontal errors of digitized  
540 contours. Journal of Spatial Science, 55:1, pp. 147-164.



- 541 Asaah, V. A., 2010. Lode gold mineralization in the Neoproterozoic granitoids of Batouri,  
542 southeastern Cameroon. Faculty of Energy and Economic Sciences, Clausthal University  
543 of Technology, Doctorat/PhD Thesis, 187 p.
- 544 Benkhelil J., Pierre G., Claude P., Ngueutchoua G., 2002. Lithostratigraphic, geophysical and  
545 morpho-tectonic studies of the South Cameroon shelf. *Marine and Petroleum Geology*,  
546 19, pp. 499-517.
- 547 Bessoles B., and Trompette M., 1980. “Géologie de l’Afrique: la chaine Panafricaine, “Zone  
548 mobile d’Afrique centrale (partie sud) et Zone mobile soudanaise”,” *Mémoire du BRGM*,  
549 vol. 92, pp. 19–80.
- 550 Blakely, R. J., 1996. *Potential theory applied in gravity and magnetism*. Cambridge University  
551 Press, Cambridge, 441p.
- 552 Cordell L. & Grauch V.J.S., 1985. Mapping basement magnetization zones from aeromagnetic  
553 data in the San Juan Basin, New Mexico. In: Hinze W.J. (ed.) – *The utility of regional  
554 gravity and magnetic anomaly maps*. Soc. Explor. Geophys., pp. 181-197.
- 555 Cornacchia M. and Dars R., 1983. “Un trait structural majeur du continent africain: Les  
556 linéaments centrafricains du Cameroun au Golfe d’Aden,” *Bulletin de la Société  
557 Géographique de France*, vol. 25, pp. 101–109.
- 558 Coyne, Bellier, 2010. Aménagement hydroélectrique de Lom Pangar, doc. No 10108-RP-400-  
559 B, pp.57-58.
- 560 Dumont J. F., 1986. “Identification par télédétection de l’accident de la Sanaga (Cameroun).  
561 Sa position dans les grands accidents d’Afrique Centrale et de la limite Nord du Craton  
562 du Congolais,” *Géodynamique*, vol. 1, no. 1, pp. 13–19.
- 563 Eno Belinga S. M., 1984. *Géologie du Cameroun*, Librairie Universitaire de Yaoundé,  
564 République Unie du Cameroun.



- 565 Gazel J., Gerard G., 1954. Geological map of Cameroon recognition at the scale 1/500 000, p.  
566 27.
- 567 KanKeu, B., Greiling, R. O., Nzenti, J. P., 2009. Pan-African strikeslip tectonics in eastern  
568 Cameroon -Magnetic fabrics (AMS) and structures in the Lom basin and its gneissic  
569 basement. - Precambrian Research, 174, pp. 258-272.
- 570 Koch, F., Wiens, D., Nyblade, A., Shore, P., Tibi, R., Ateba, B., Tabod, C. and Nnange, J.,  
571 2012. Upper Mantle Anisotropy beneath the Cameroon Volcanic Line and Congo Craton  
572 from Shear Wave Splitting Measurements. Geophysical Journal International, 190, pp.  
573 75-86.
- 574 Kouske, A.P. 2006. Geological and environmental study of the artisanal gold mining sector of  
575 Bangbel-Mborguéne (East Cameroon), DEA dissertation in earth sciences, University of  
576 Yaounde I, Cameroon, 89 p.
- 577 Mboudou G. M., Kennedy F. F., Njoh O. A., Agyingi C. M., 2017. Characterization of Alluvial  
578 Gold Bearing Sediments of Betare Oya District-East Cameroon, Implication for Gold  
579 Exploration and Recovery. Journal of Geology, 2017, 7, pp. 1724-1738.
- 580
- 581 Miller, H. G., Singh, V., 1994. Potential field tilt- a new concept for location of potential field  
582 sources. Journal of applied Geophysics, 32, pp. 213-217.
- 583 Ndougsa-Mbarga, T. E., Campos-Enriquez J. O. and Yene-Atangana J. Q., 2007. Gravity  
584 anomalies, sub-surface structure and oil and gas migration in the Mamfe, Cameroon-  
585 Nigeria, sedimentary basin. Geofísica Internacional, 46, pp. 129-139.
- 586 Ndougsa, M.T., Bikoro B. A., Tabod C. T., Sharma K. K., 2013. Filtering of gravity and  
587 magnetic anomalies using the finite element approach (fea). Journal of Indian geophysical  
588 union.





- 589 Ngako, V., Affaton, P., Nnange, J. M., Njanko, Th., 2003. Pan-African tectonic evolution in  
590 central and Southern Cameroon: transpression and transtension during sinistral shear  
591 movements, *J. Afr. Earth Sci.*, 36, pp. 207-214.
- 592 Nih Fon, A., Bih, C. V., Suh, C. E., 2012. Application of Electrical Resistivity and  
593 Chargeability Data on a GIS Platform in Delineating Auriferous Structures in a Deeply  
594 Weathered Lateritic Terrain, Eastern Cameroon. *International Journal of Geosciences*, pp.  
595 960-971.
- 596 Odey Omang B., Che V. B., Nih Fon, Embui V., Cheo Suh E., 2014. Regional Geochemical  
597 Stream Sediment Survey for Gold Exploration in the Upper Lom Basin, Eastern  
598 Cameroon. *International Journal of Geosciences*, 2014, 5, pp. 1012-1026.
- 599 Owono Amougou O., Ndougsa Mbarga T., Meying Arsène, Assembe S. P., Ngho J. D.,  
600 Ngoumou P. C., and Yandjimain J., 2019. Evidence of Major Structural Features over the  
601 Pan-African Domain in the Bertoua-Mbangue Area (East Cameroon) from a Multiscale  
602 Approach of Modeling and Interpretation of Aeromagnetic Data. *International Journal of*  
603 *Geophysics Volume 2019*, Article ID 9148678, 12 p.
- 604 Paterson, Grant, Watson Ltd., 1976. Aeromagnetic studies on some regions of the United  
605 Republic of Cameroon. Interpretation report. A.C.D.I. Toronto, 192 p.
- 606 Poidevin, J. L., 1985. “Le Protérozoïque supérieur de la République Centrafricaine,” *Annals*  
607 *of Royal Museum for Central Africa*, Tervuren, vol. 91, p. 74.
- 608 Rasmussen, R. and Pedersen, L.B., 1979. End corrections in potential field modeling, *Geophys.*  
609 *Prospect.*, 27, pp. 749–760.
- 610 Regnault, J.M., 1986. *Geological Synthesis of Cameroon*. 119 p.



- 611 Reid, A. B., Allsop, J.M. Granser, H., Millett, A. J., and Somerton. I. W., 1990. Magnetic  
612 interpretation in three dimensions using Euler Deconvolution: *Geophysics*, vol.55, pp.  
613 80-90.
- 614 Rolin P., 1995. “La zone de décrochement panafricain des oubanguides en république  
615 centrafricaine,” *Comptes Rendus de l’Académie des Sciences*, vol. 320, no. 2A, pp. 63–  
616 69.
- 617 Salem,A., William, S., Fairhead, D., Ravat, D, Smith, R., 2007. Tilt-depth method: a simple  
618 depth estimation method using first-order magnetic derivatives. *The Leading Edge*  
619 December, Meter Reader, 150, pp. 2-5.
- 620 Salem, A., Williams, S., Fairhead, J.D., Smith, R., Ravat, D.J., 2008. Interpretation of magnetic  
621 data using tilt-angle derivatives. *Geophysics* 73, P.L1–P.L10.
- 622 Shandini N. Y., Tadjou J. M., and Basseka C. A., 2011. “Delineating deep basement faults in  
623 South Cameroon area,” *World Applied Sciences Journal*, vol. 14, no. 4, pp. 611–615.
- 624 Skalbeck, J.D., Karlin, R.E., Shevenell, L. and Widmer, M.C., 2005. Gravity and aeromagnetic  
625 modeling of alluvial basins in the southern Truckee Meadows adjacent to the Steamboat  
626 Hills geothermal area, Washoe County, Nevada. *Geophysics*, Vol. 70, N°3.
- 627 Soba, D., 1989. The Lom series: geological and geochronological study of a volcano-  
628 sedimentary basin of the Pan-African chain in eastern Cameroon. State Doctorate Thesis,  
629 Pierre and Marie Curie University, Paris 6, 198 p.
- 630 Tadjou J. M., Manguelle-Dicoum E., Tabod C. T., 2004. “Gravity modelling along the  
631 northern margin of the Congo craton, South-Cameroon,” *Journal of the Cameroon*  
632 *Academy of Sciences*, vol. 4, pp. 51–60.
- 633 Thompson D.T., 1982. EULDPH: A new technique for making computer-assisted depth  
634 estimates from Magnetic data. *Geophysics*, vol.47, pp.31-37.



635 Toteu S. F., Penaye J., and Poudjom Djomani Y., 2004. Geodynamic evolution of the Pan-African  
636 belt in central Africa with special reference to Cameroon. Canadian Journal of Earth  
637 Sciences Vol. 41, pp.73-85.

638 Verduzco, B., Fairhead, J. D, Green, C. M., Mackenzie, C., 2004. New insights into magnetic  
639 derivatives for structural mapping. The Leading Edge, SEG February, pp. 116-119.

640 Won, I.J. and Bevis, M., 1987. Computing the gravitational and magnetic anomalies due to a  
641 polygon: Algorithms and FORTRAN subroutines, Geophysics, 52, 232–238.

642

643